PNAS

Supporting Information for

A Wireless, Implantable Bioelectronic System for Monitoring Urinary Bladder Function Following Surgical Recovery

Jihye Kim, Matthew I. Bury, Kyeongha Kwon, Jae-Young Yoo, Nadia V. Halstead, Hee-Sup Shin, Shupeng Li, Sang Min Won, Min-Ho Seo, Yunyun Wu, Do Yun Park, Mitali Kini, Jean Won Kwak, Surabhi R. Madhvapathy, Joanna L. Ciatti, Jae Hee Lee, Suyeon Kim, Hanjun Ryu, Kento Yamagishi, Hong-Joon Yoon, Sung Soo Kwak, Bosung Kim, Yonggang Huang, Lisa C. Halliday, Earl Y. Cheng, Guillermo A. Ameer*, Arun K. Sharma*, John A. Rogers*

* Corresponding author: Guillermo A. Ameer, Arun K. Sharma, John A. Rogers
Email: g-ameer@northwestern.edu, arun-sharma@northwestern.edu, jrogers@northwestern.edu

This PDF file includes:

Supporting text
Figures S1 to S32
Tables S1

Supporting Information Text

Rodent Urine Measurements Using the Filter Paper Method. This method served to accurately and reproducibly quantify the volumes associated with urination events (Fig. 3*F* and *SI Appendix*, Fig. S12) of an animal with an implanted monitoring system, placed in a transparent cage. A smartphone placed under the cage captures video of filter wetting with urine. A calibration process used known amounts of DI water delivered to the filter paper (*SI Appendix*, Fig. S13). The experiments involved continuous measurements for a period of 6 h (Fig. 3*G*), during which four large and small urinations occurred. The relative changes in resistance of the strain gauge correspond well with the volume of urine determined using this filter paper method.

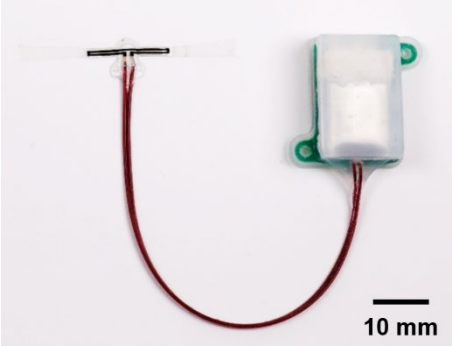

Fig. S1. Photograph of the bladder monitoring system.

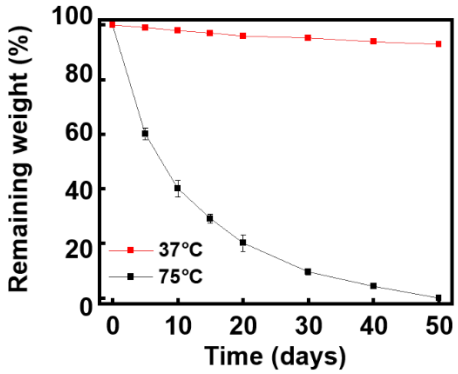

Fig. S2. Remaining weight of the bioresorbable strain gauge as a function of time in PBS solution (pH = 7.4) at 37 °C and 75 °C.

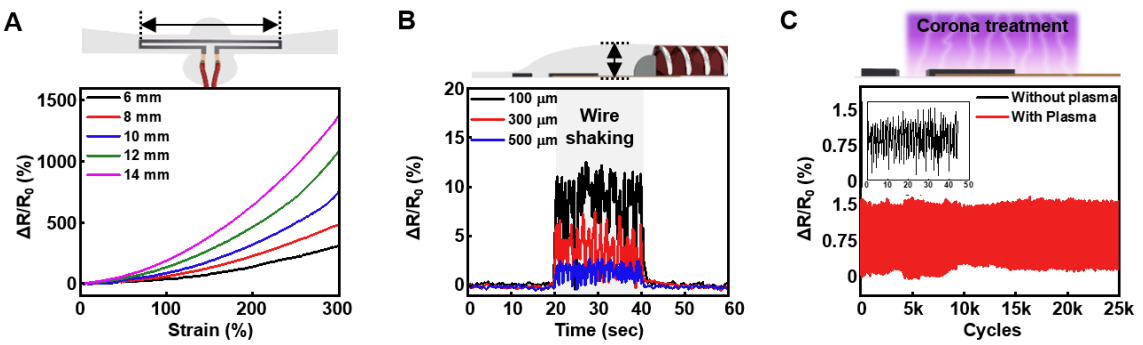

Fig. S3. Characterization of the strain gauge system (*A*) Relative change in resistance of the strain gauge as a function of strain for devices with various lengths of carbon black doped silicone elastomer. (*B*) Relative change in resistance of the strain gauge with various thicknesses of silicone elastomer coatings on the connection between the wire and the Cu/PI electrode while mechanically shaking the wire. (*C*) Bending cyclic test of a strain gauge system fabricated with and without corona treatment.

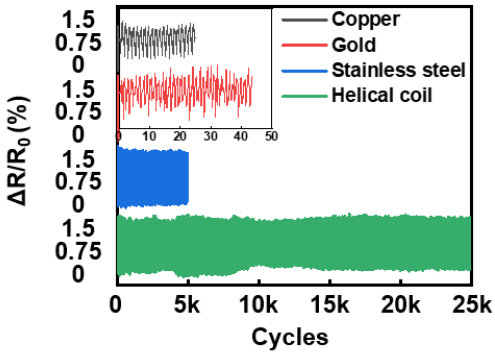

Fig. S4. Bending cyclic test of strain gauge systems with various types of interconnecting wire.

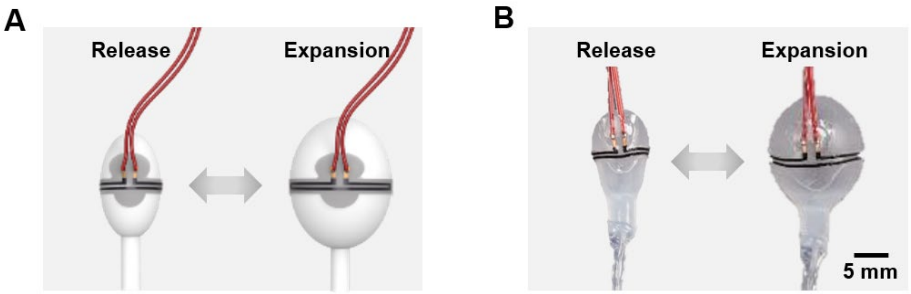

Fig. S5. (*A*) Schematic illustration and (*B*) photograph of a benchtop setup with a mimic rat bladder model.

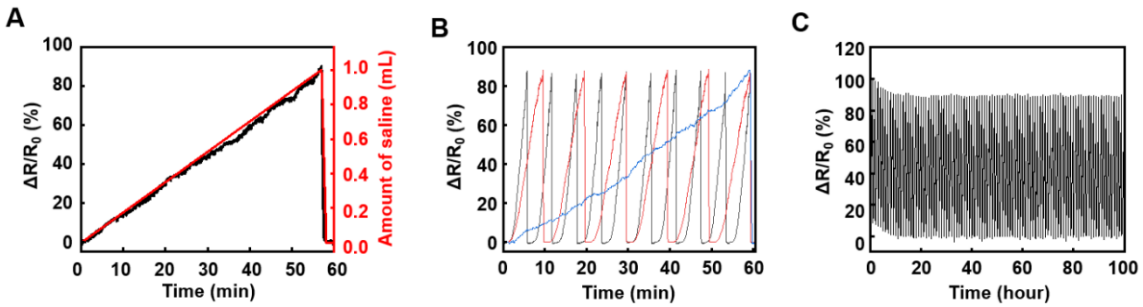

Fig. S6. (*A*) Relative change in resistance of a strain gauge on a mimic bladder during injection of saline solution. (*B*) Relative change in resistance of a strain gauge at different injection rates. (*C*) Cyclic test for 100 h.

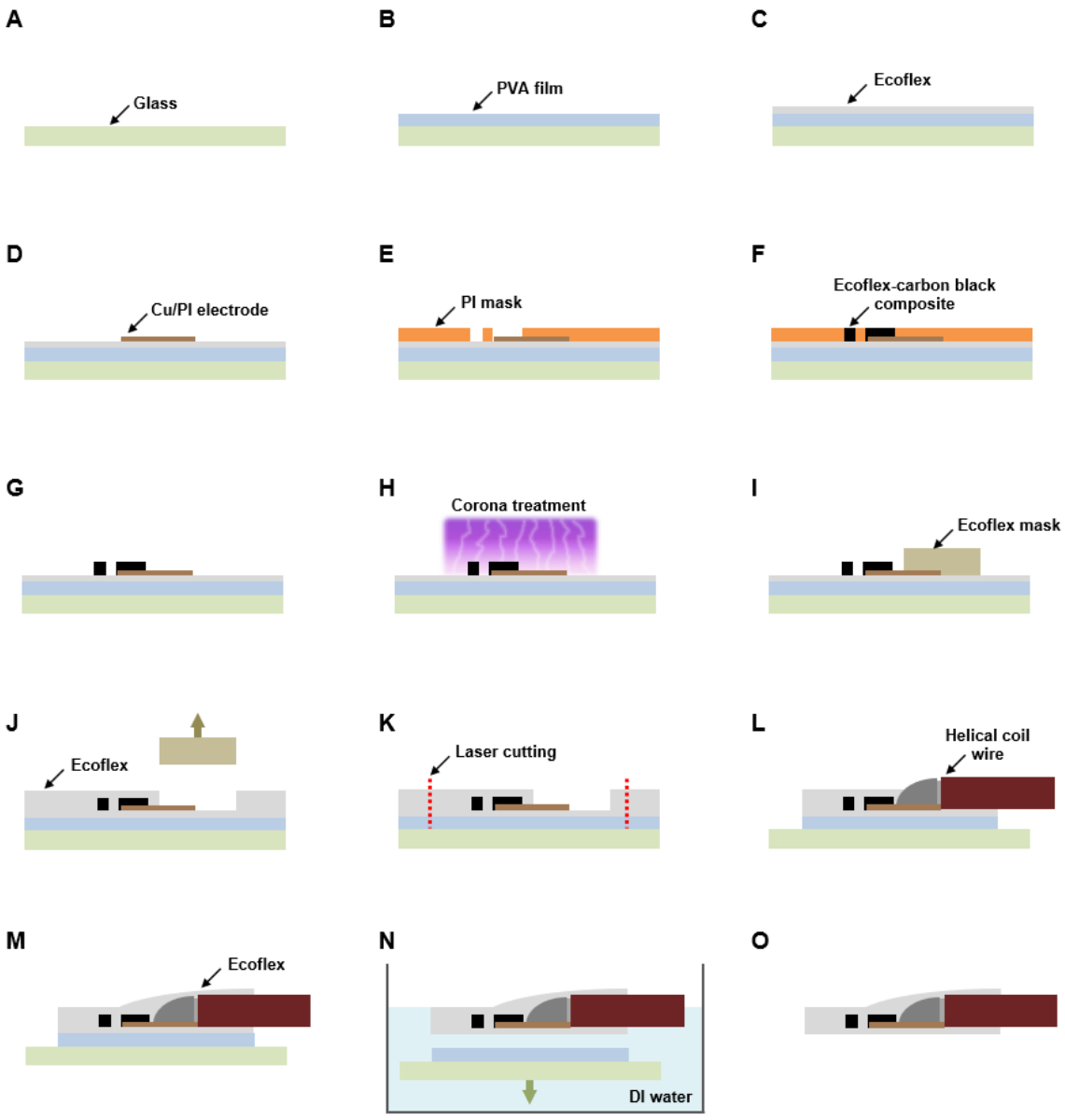

Fig. S7. Process for fabricating the strain gauge. (*A*) Preparation of a glass substrate. (*B*) Attachment of a PVA film. (*C*) Spin-coating of a silicone elastomer. (*D*) Attachment of the Cu/PI electrode. (*E*) Attachment of the PI mask. (*F*) Screen-printing of a carbon black doped silicone elastomer. (*G*) Removal of the PI mask. (*H*) Corona treatment of the carbon black doped silicone elastomer and Cu/PI electrode. (*I*) Attachment of a silicone elastomer mask on the Cu/PI electrode. (*J*) Spin-coating of a silicone elastomer and removal of the PDMS mask. (*K*) Laser cutting of the strain gauge outline. (*L*) Soldering of a helical coil wire to the Cu/PI electrode. (*M*) Coverage of silicone elastomer on the solder joint to the wire. (*N*) Dissolution of the PVA film with DI water. (*O*) Completed strain gauge.

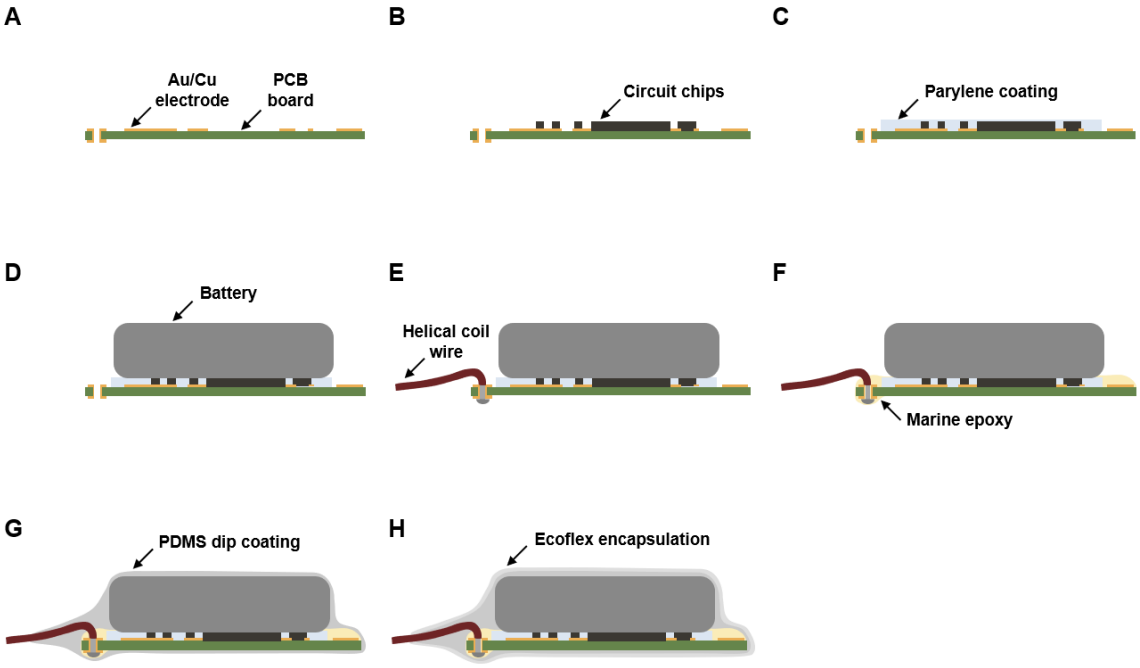

Fig. S8. Process for fabricating the base station. (*A*) Preparation of a PCB with a Au/Cu electrode. (*B*) Soldering of circuit components. (*C*) Parylene coating of the PCB. (*D*) Soldering of the battery. (*E*) Soldering of the helical coil wire. (*F*) Covering the soldered parts with marine epoxy. (*G*) PDMS dip coating. (*H*) Silicone elastomer encapsulation with a 3D-printed mold.

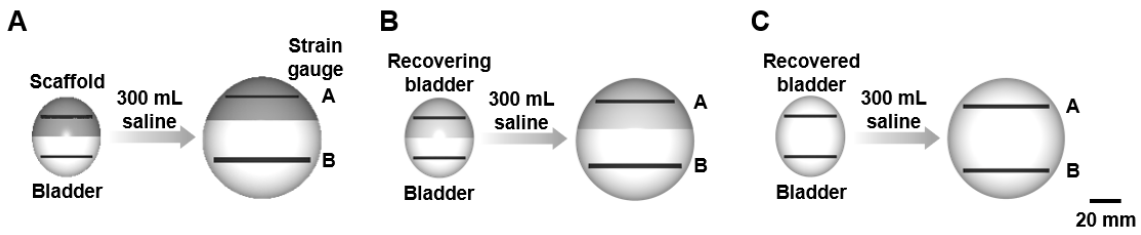

Fig. S9. FEM simulation setups for three models after partial cystectomy and scaffold implantation. (*A*) The first model corresponds to the case after suturing the scaffold to the upper part of the resected bladder, with normal bladder tissue in the lower part. (*B*) The second model corresponds to partial regeneration of bladder tissue with the scaffold. (*C*) The third model corresponds to fully regenerated bladder tissue and fully bioresorbed scaffold.

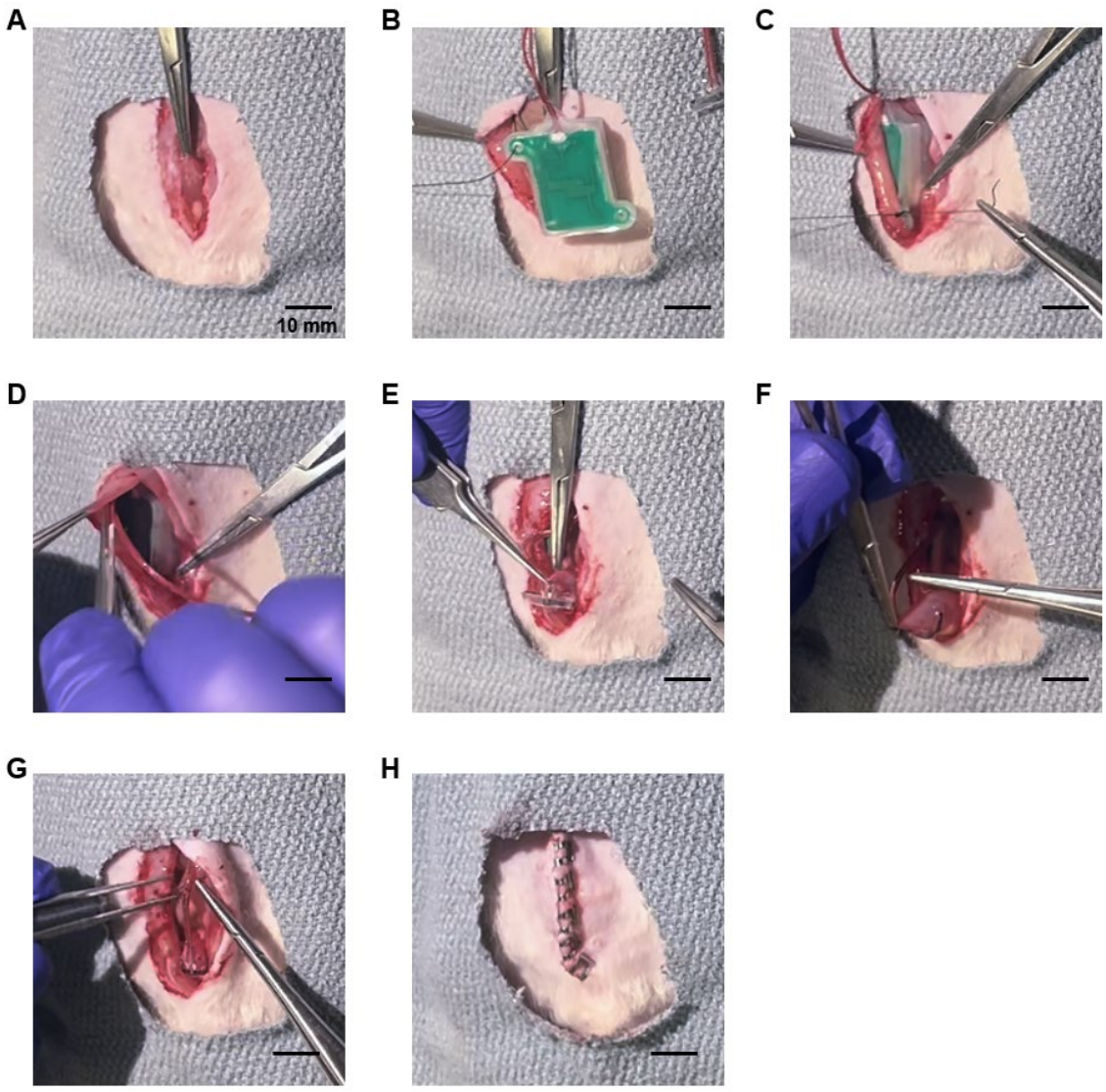

Fig. S10. Detailed surgical procedure for experiments with rat models. (*A*) Open the skin and abdominal wall for implantation of the strain gauge system. Suture the (*B*) first and (*C*) second suture holes of the base station to the abdominal wall. (*D*) Place the helical coil wire into the abdomen. (*E*) Suture the strain gauge on the front side of bladder wall. (*F*) Suture the strain gauge on the back side of bladder wall. (*G*) Suture the wire to the abdominal wall. (*H*) Close the abdominal wall and skin with suture and surgical staples.

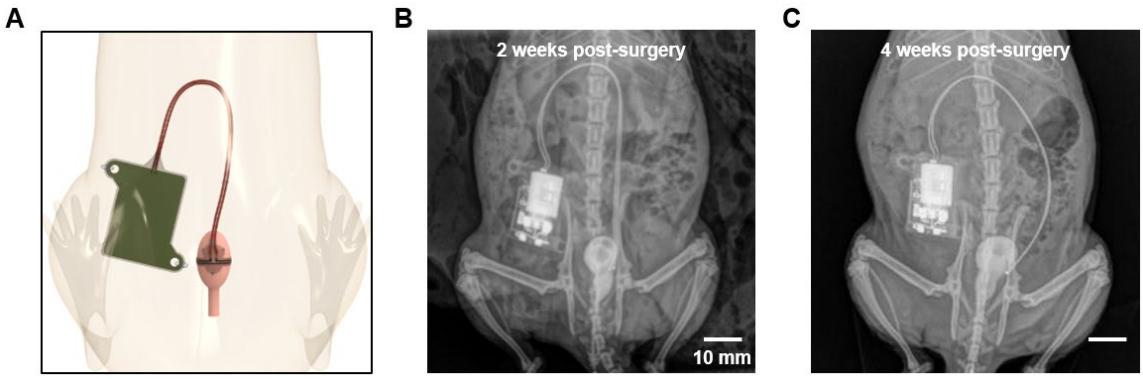

Fig. S11. (*A*) Image showing the strain gauge implanted on the bladder wall of rat. (*B, C*) X-ray images of urodynamic study after 2 and 4 weeks post-surgery.

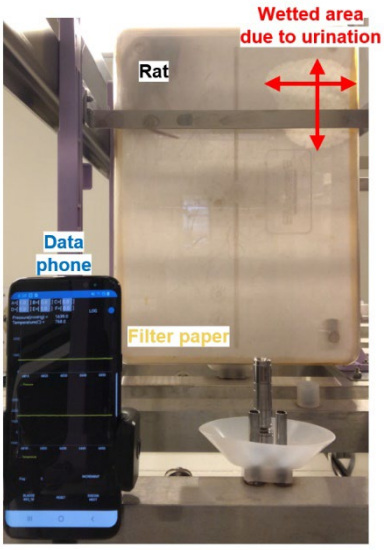

Fig. S12. Image of a smartphone for urine measurements using the filter paper method.

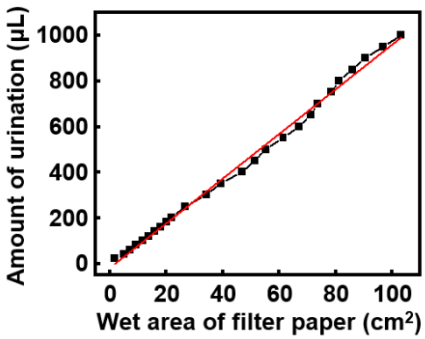

Fig. S13. Amount of urine as a function of the wetting area of a piece of filter paper.

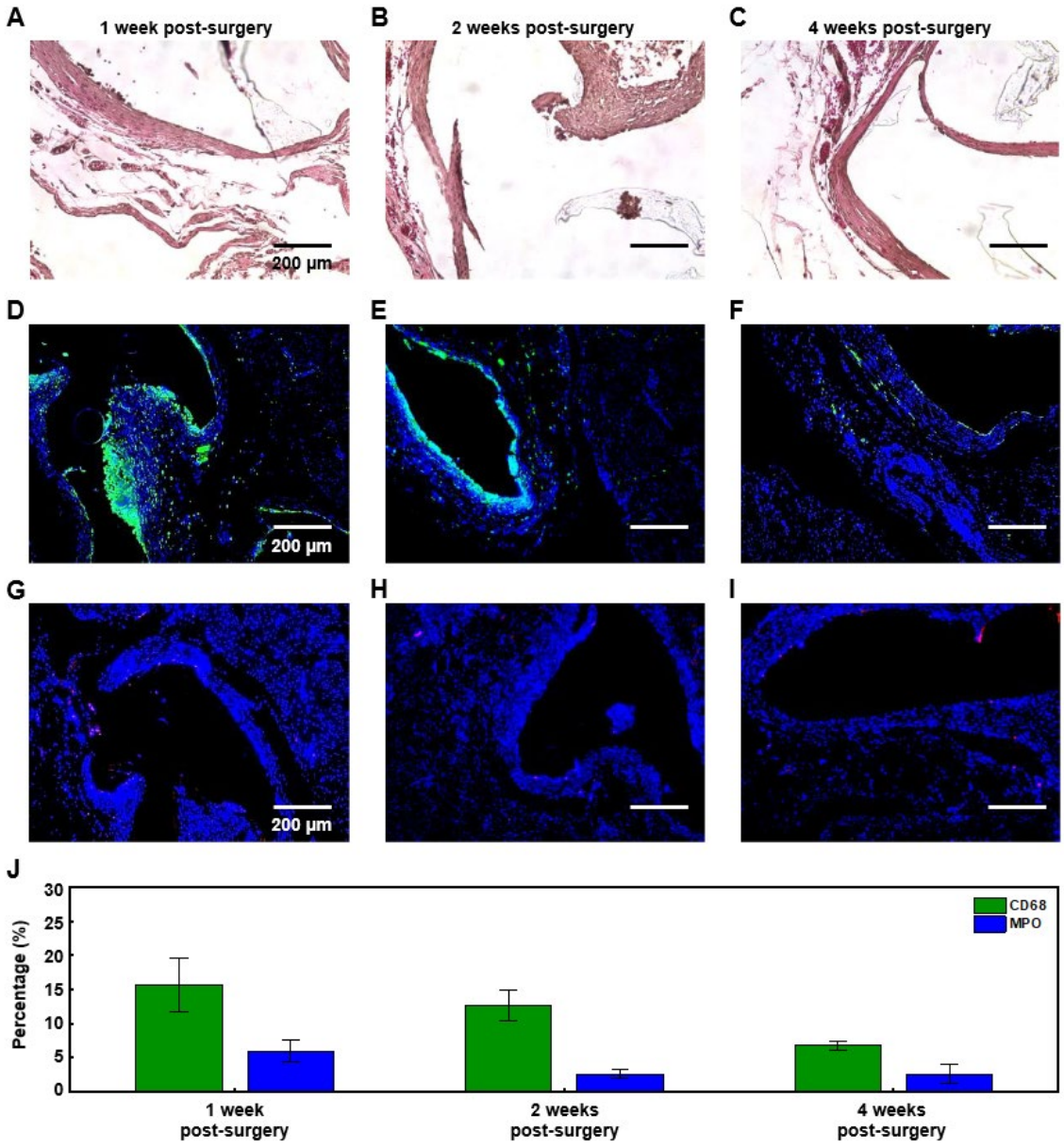

Fig. S14. Biocompatibility studies in a rat model. (*A-C*) Images for H&E after 1, 2, and 4 weeks post-surgery. (*D-F*) Images for CD68 after 1, 2, and 4 weeks post-surgery. (*G-I*) Images for MPO after 1, 2, and 4 weeks post-surgery. (*J*) Quantitative histological evaluation of CD68 and MPO after 1, 2, and 4 weeks post-surgery.

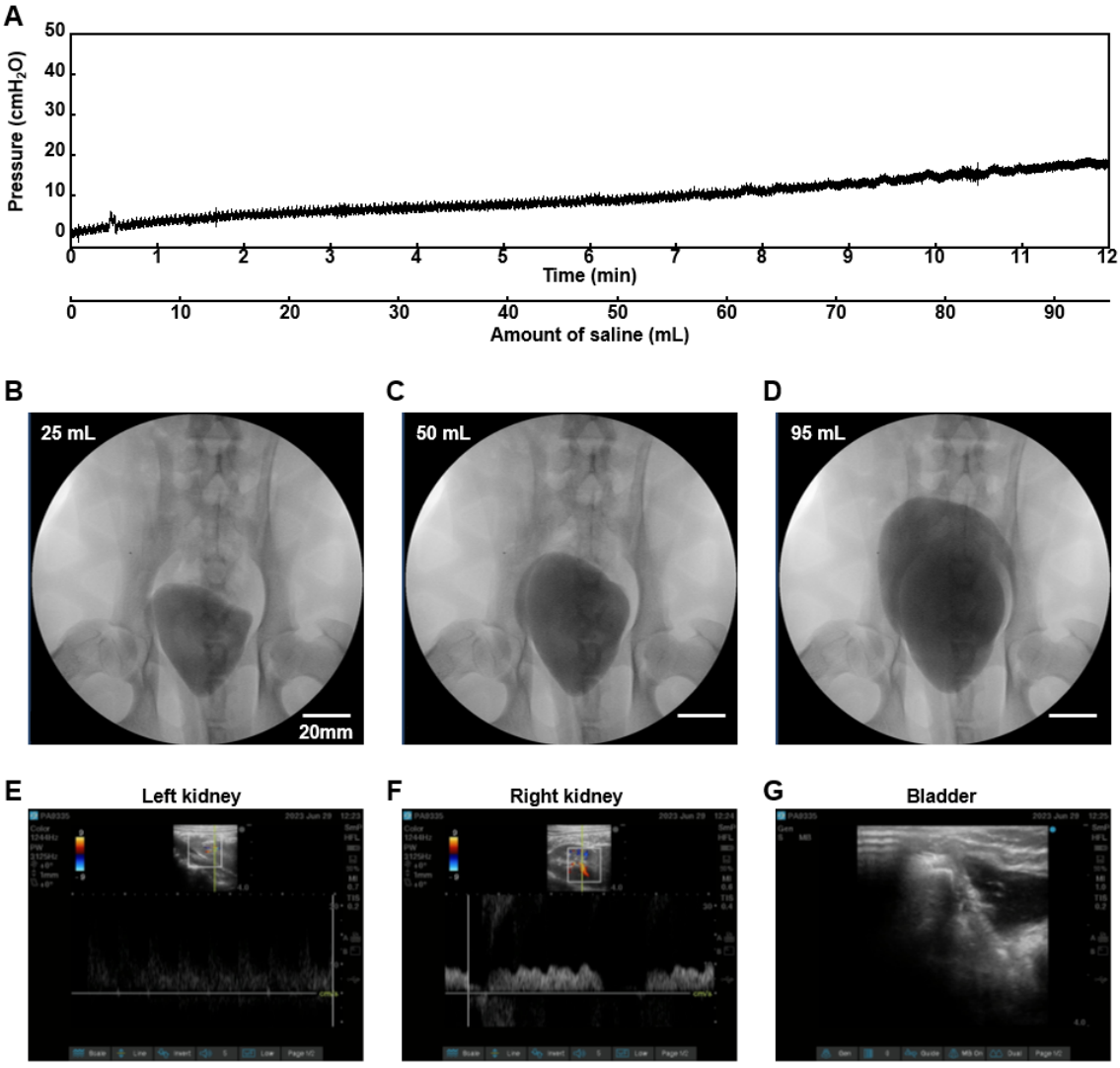

Fig. S15. Preoperative urodynamics studies of normal baboon bladder. (*A*) Bladder pressure measured by the physiological pressure transducer during saline injection. (*B-D*) C-arm fluoroscopic images after instillation of 25, 50, and 95 mL of saline solution into the bladder. (*E-G*) Ultrasound images for left and right kidney, and bladder.

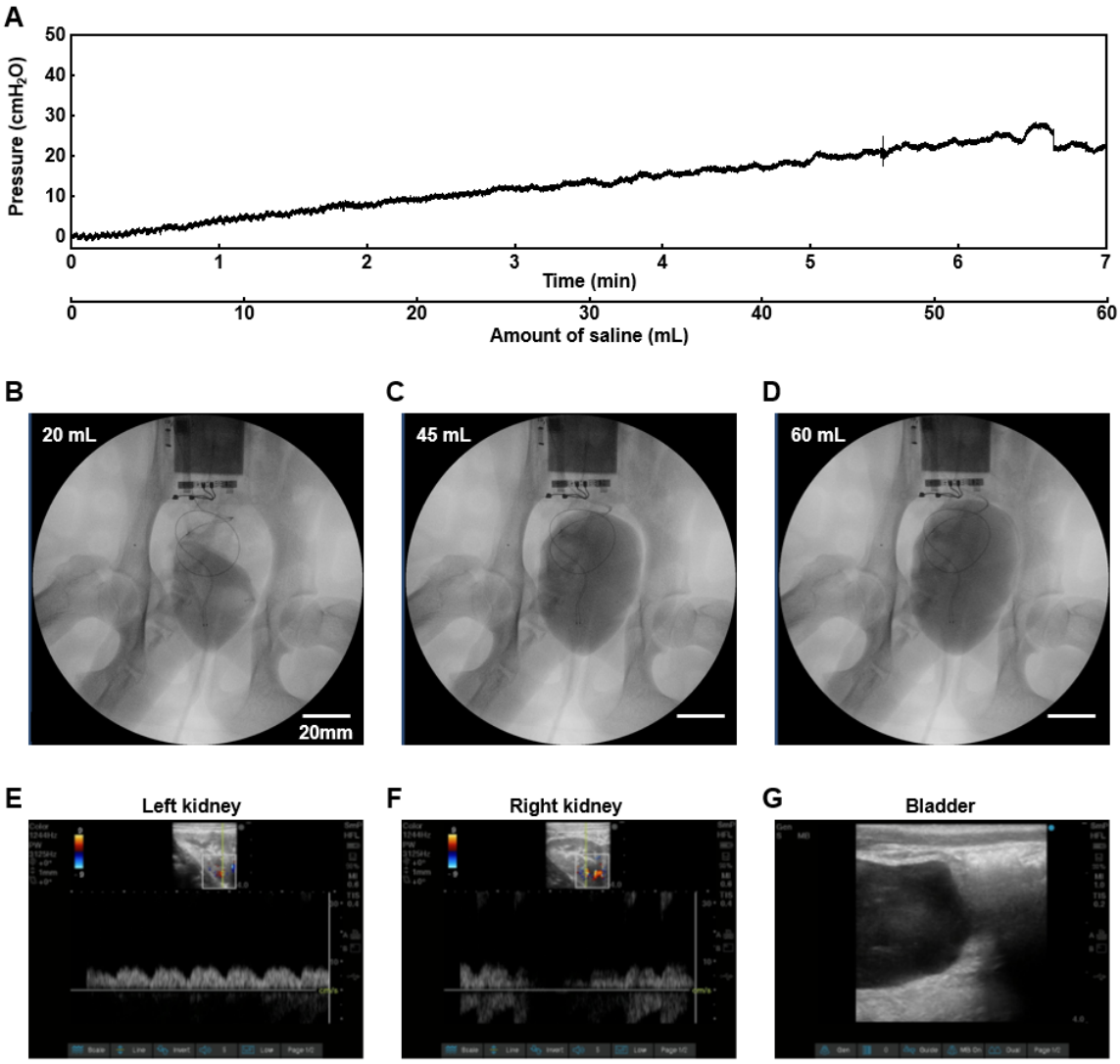

Fig. S16. Urodynamics studies 6 weeks post-surgery of normal baboon bladder. (*A*) Bladder pressure measured by the physiological pressure transducer during saline injection. (*B-D*) C-arm fluoroscopic images after instillation of 20, 45, and 60 mL of saline solution into the bladder. (*E-G*) Ultrasound images for left and right kidney, and bladder.

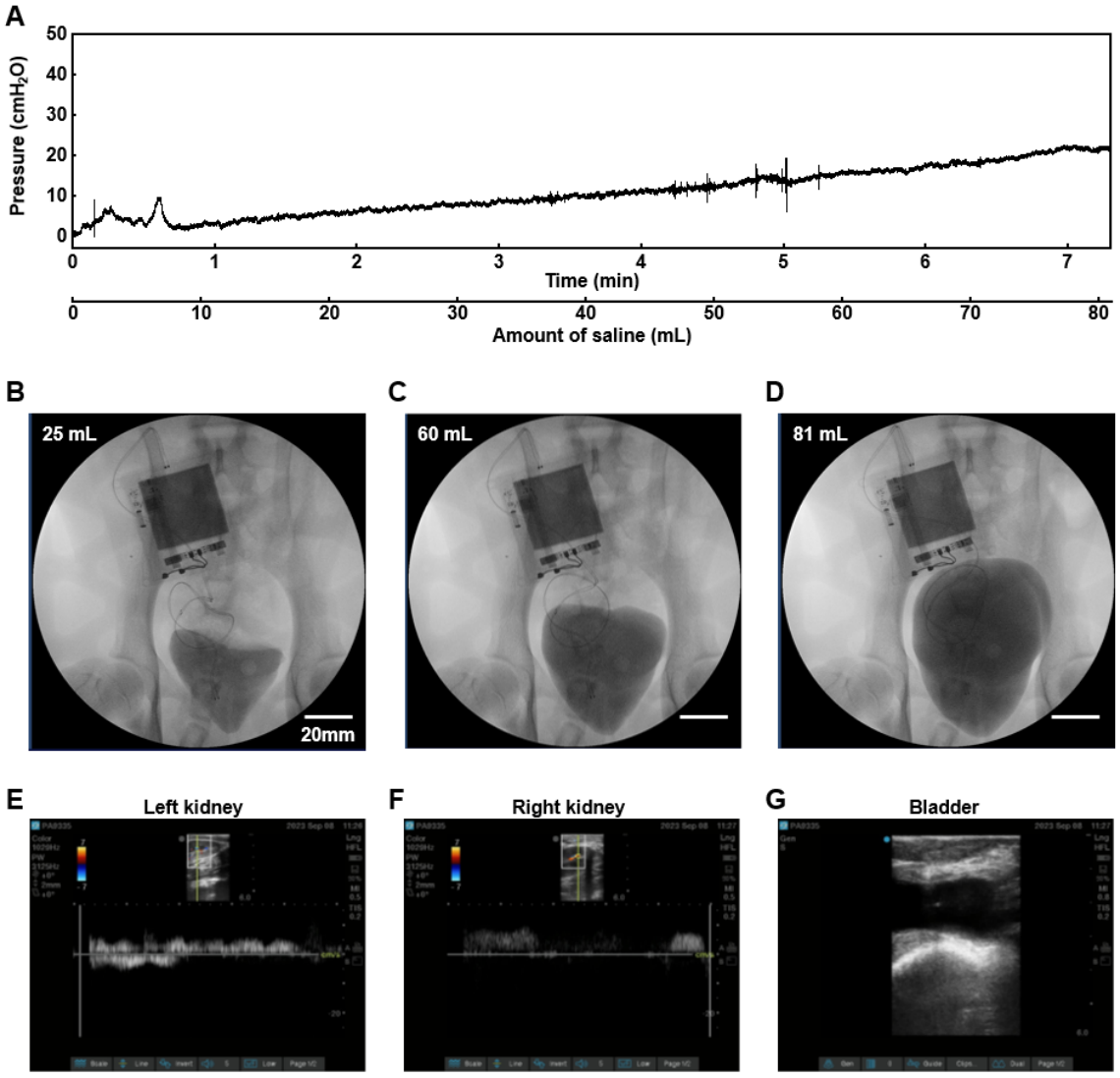

Fig. S17. Urodynamics studies 10 weeks post-surgery of normal baboon bladder. (*A*) Bladder pressure measured by the physiological pressure transducer during saline injection. (*B-D*) C-arm fluoroscopic images after instillation of 25, 60, and 81 mL of saline solution into the bladder. (*E-G*) Ultrasound images for left and right kidney, and bladder.

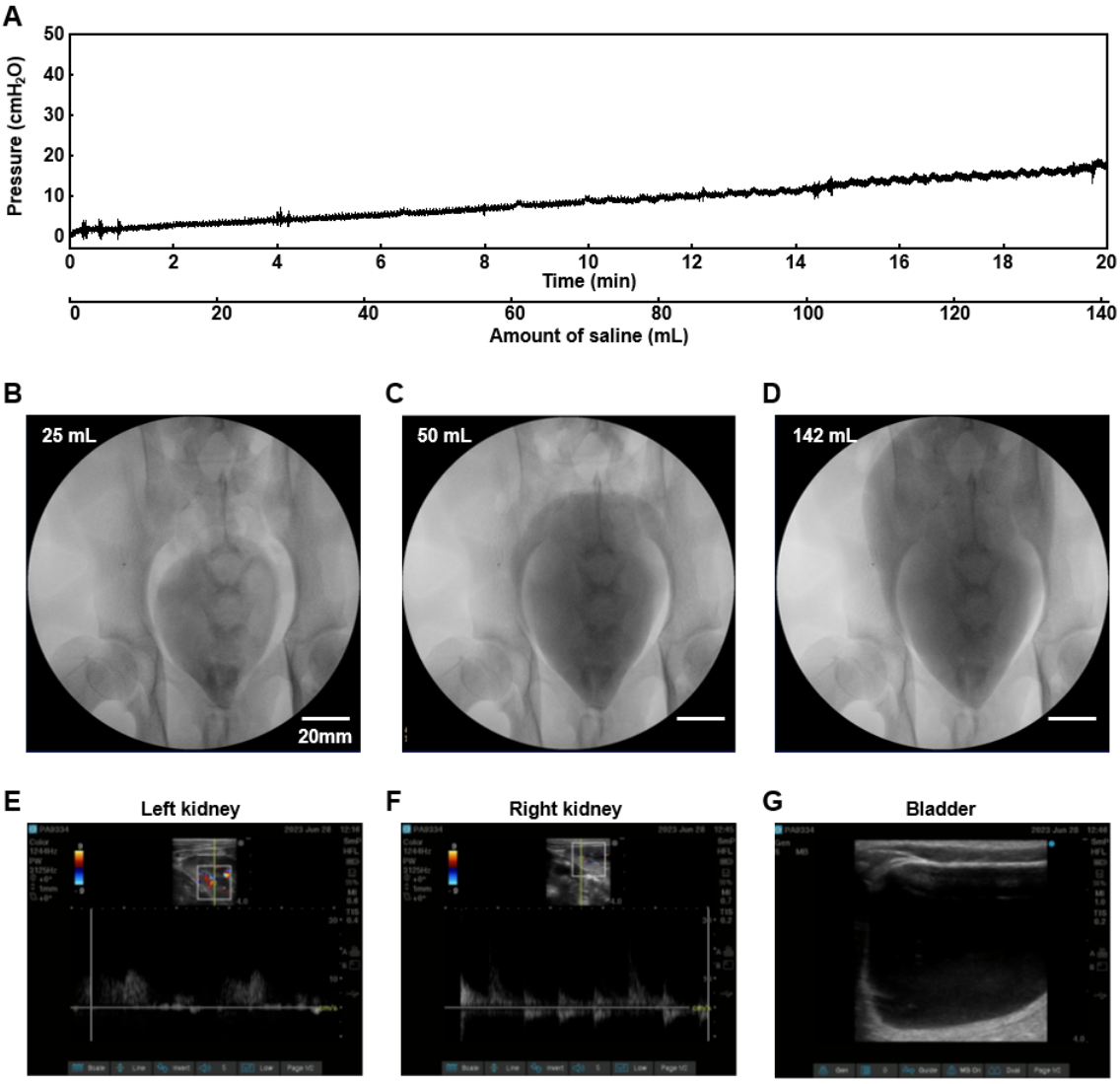

Fig. S18. Uro Preoperative urodynamics studies of baboon bladder that underwent partial cystectomy. (*A*) Bladder pressure measured by the physiological pressure transducer during saline injection. (*B-D*) C-arm fluoroscopic images after instillation of 25, 50, and 142 mL of saline solution into the bladder. (*E-G*) Ultrasound images for left and right kidney, and bladder.

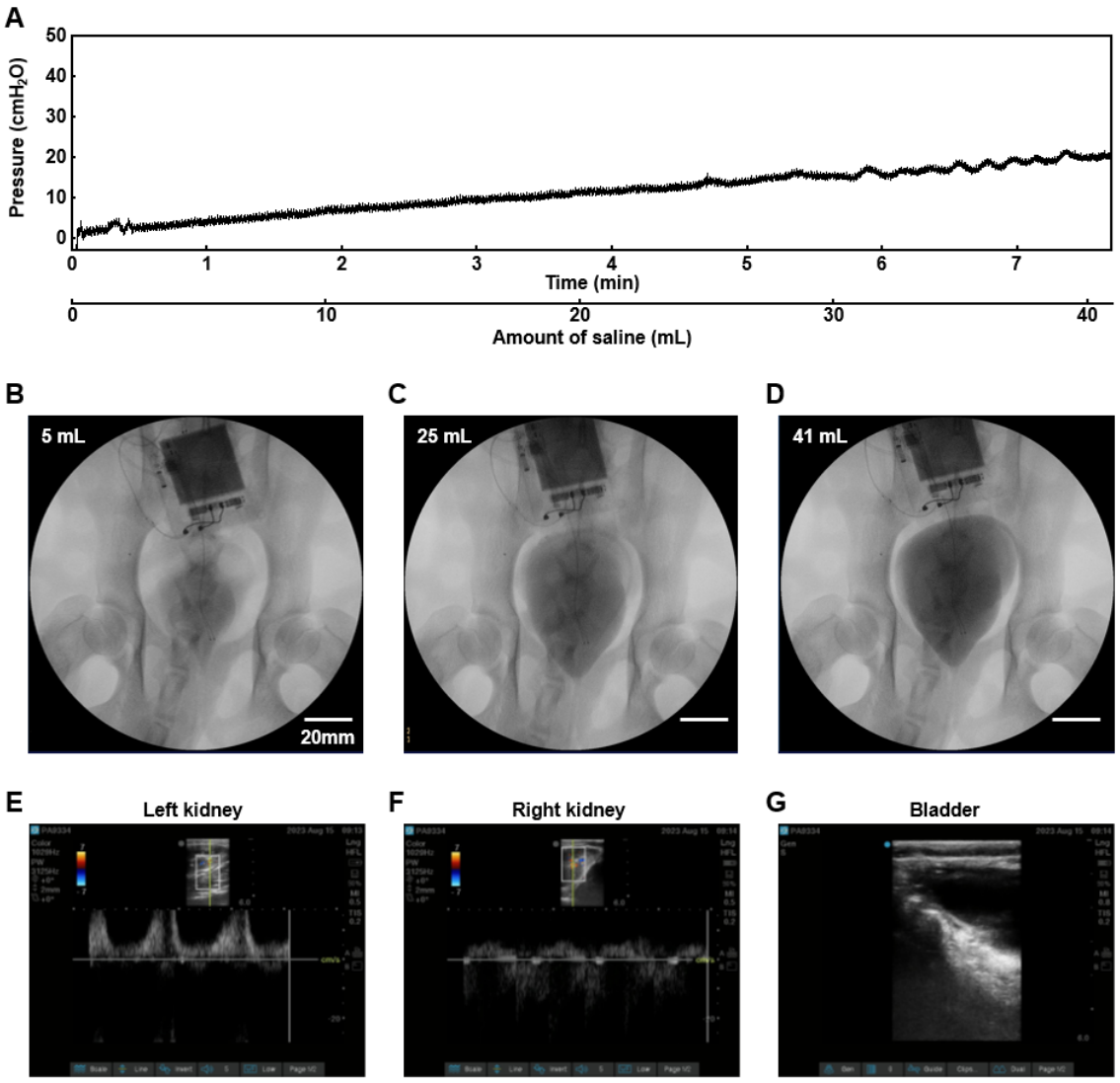

Fig. S19. Urodynamics studies 6 weeks post-surgery of bladder that underwent the partial cystectomy in a baboon model. (*A*) Bladder pressure measured by the physiological pressure transducer during saline injection. (*B-D*) C-arm fluoroscopic images after instillation of 5, 25, and 41 mL of saline solution into the bladder. (*E-G*) Ultrasound images for left and right kidney, and bladder.

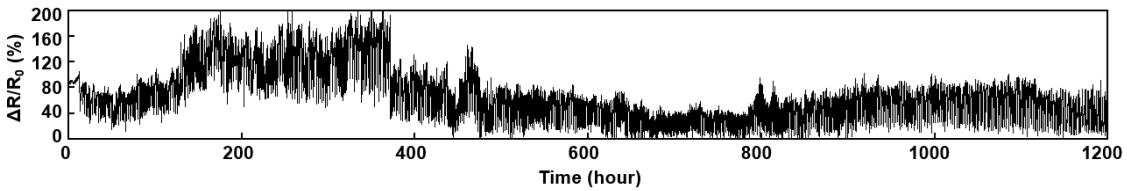

Fig. S20. Relative change in the resistance of the strain gauge, presented as raw data without baseline correction.

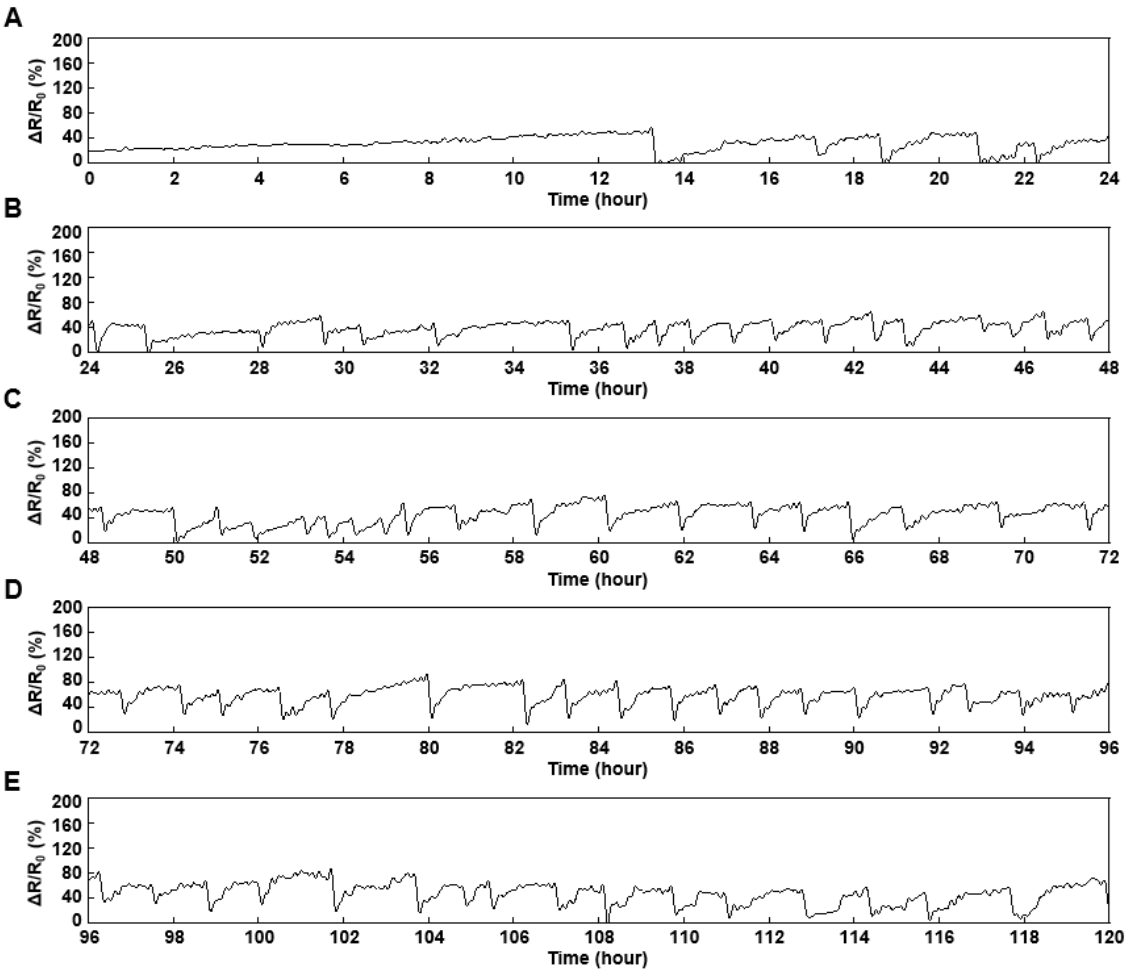

Fig. S21. Relative change in the resistance of the strain gauge from 0 h to 120 h post-surgery.

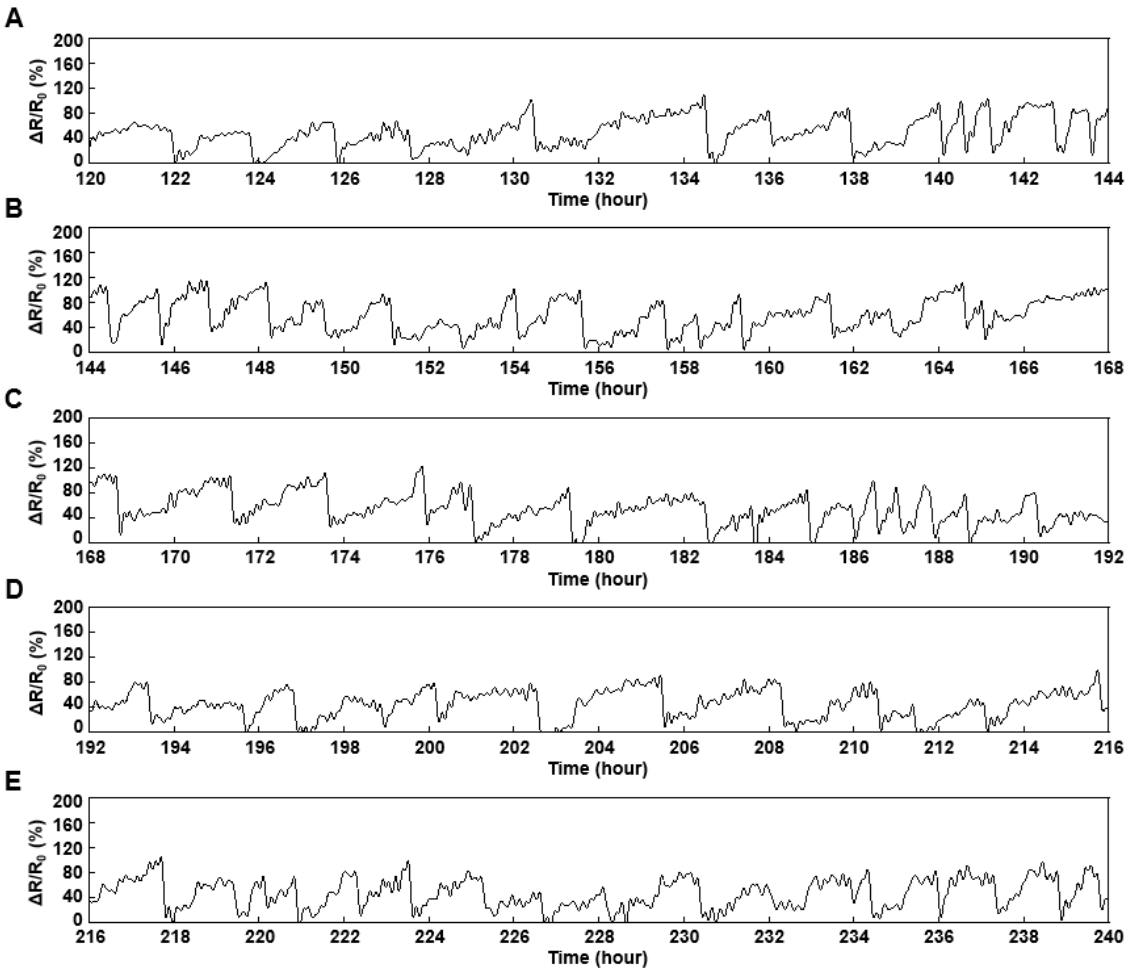

Fig. S22. Relative change in the resistance of the strain gauge from 120 h to 240 h post-surgery.

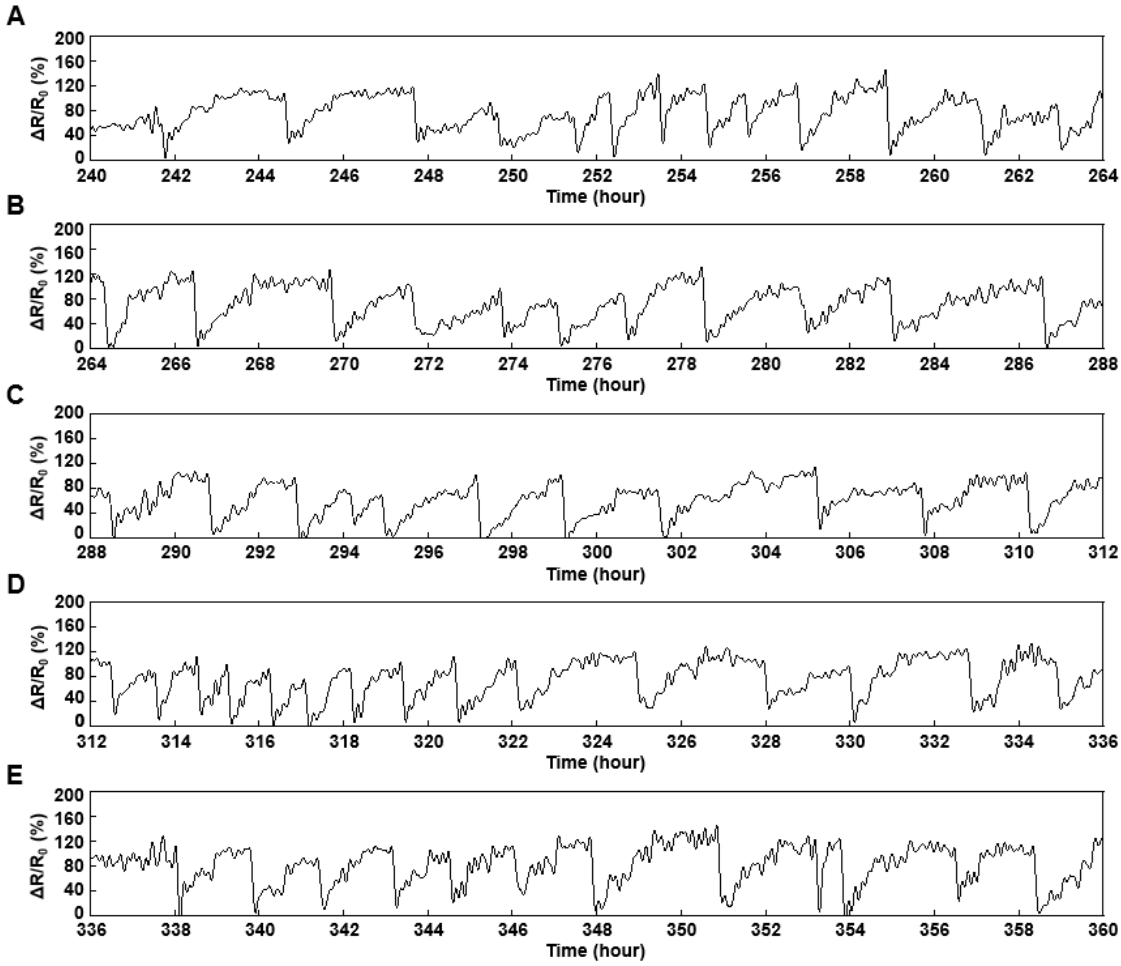

Fig. S23. Relative change in the resistance of the strain gauge from 240 h to 360 h post-surgery.

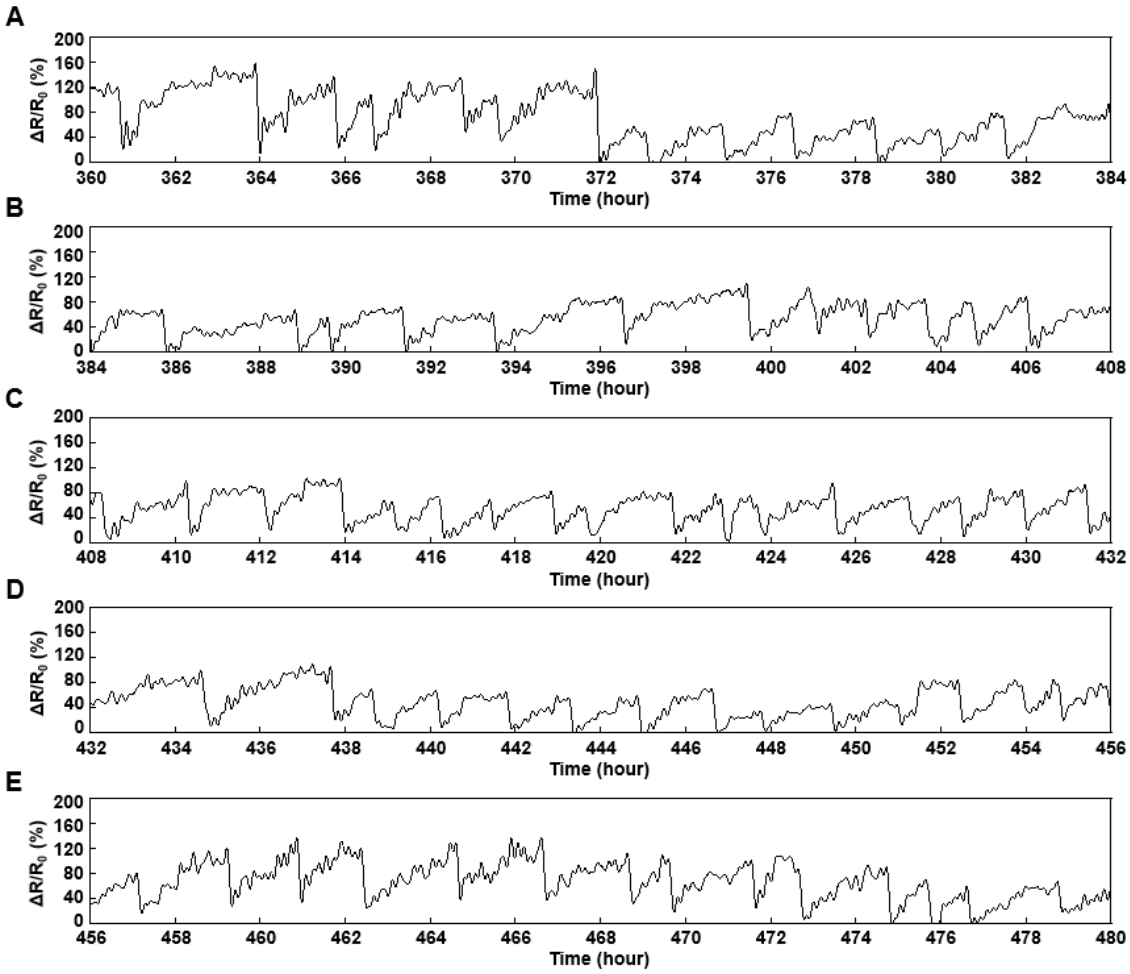

Fig. S24. Relative change in the resistance of the strain gauge from 360 h to 480 h post-surgery.

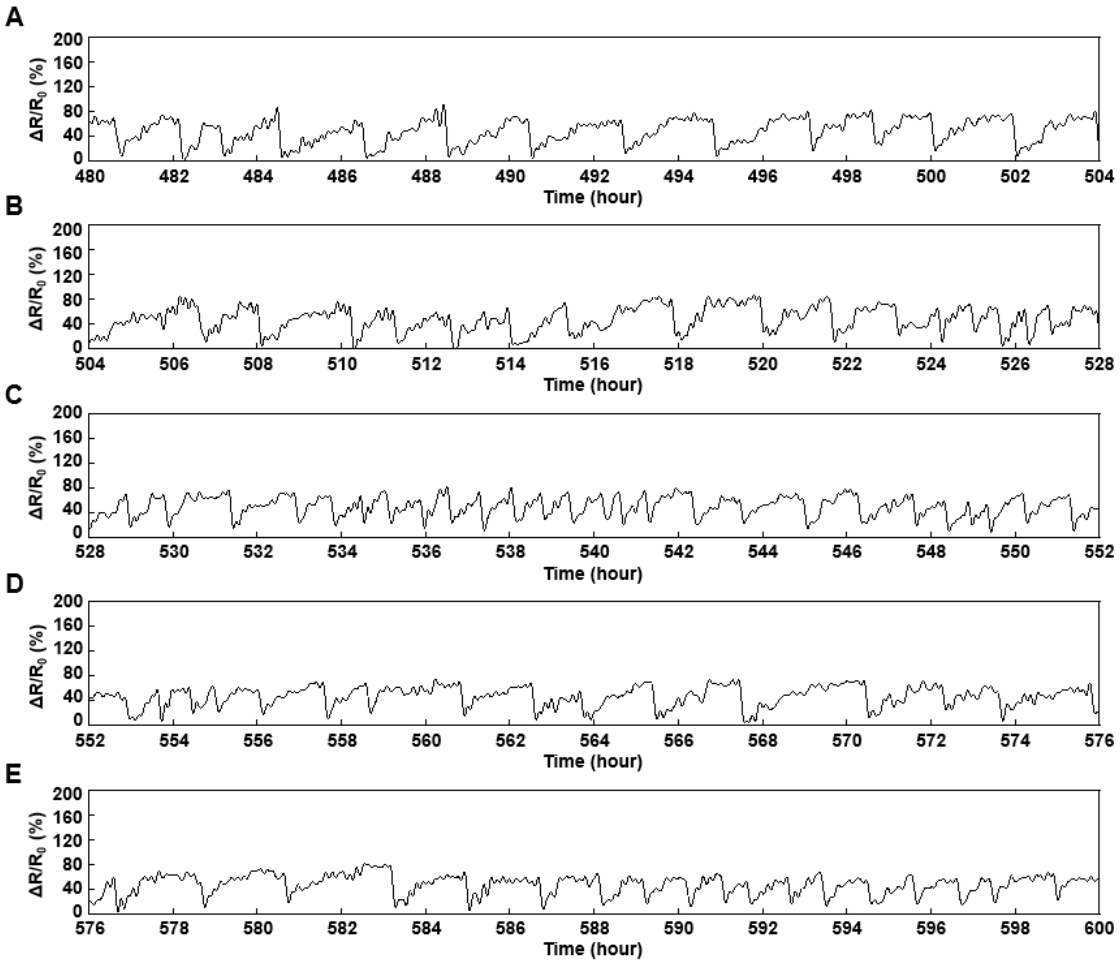

Fig. S25. Relative change in the resistance of the strain gauge from 480 h to 600 h post-surgery.

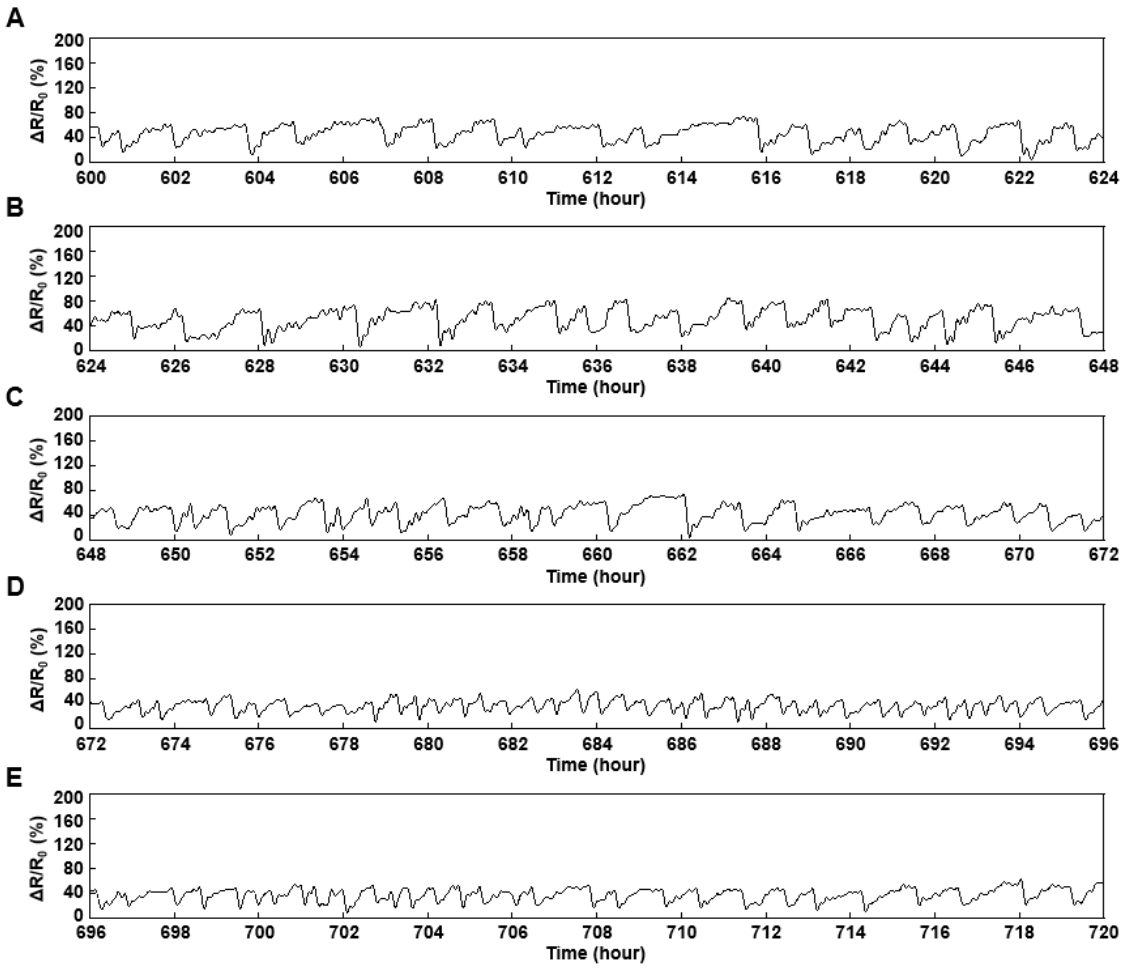

Fig. S26. Relative change in the resistance of the strain gauge from 600 h to 720 h post-surgery.

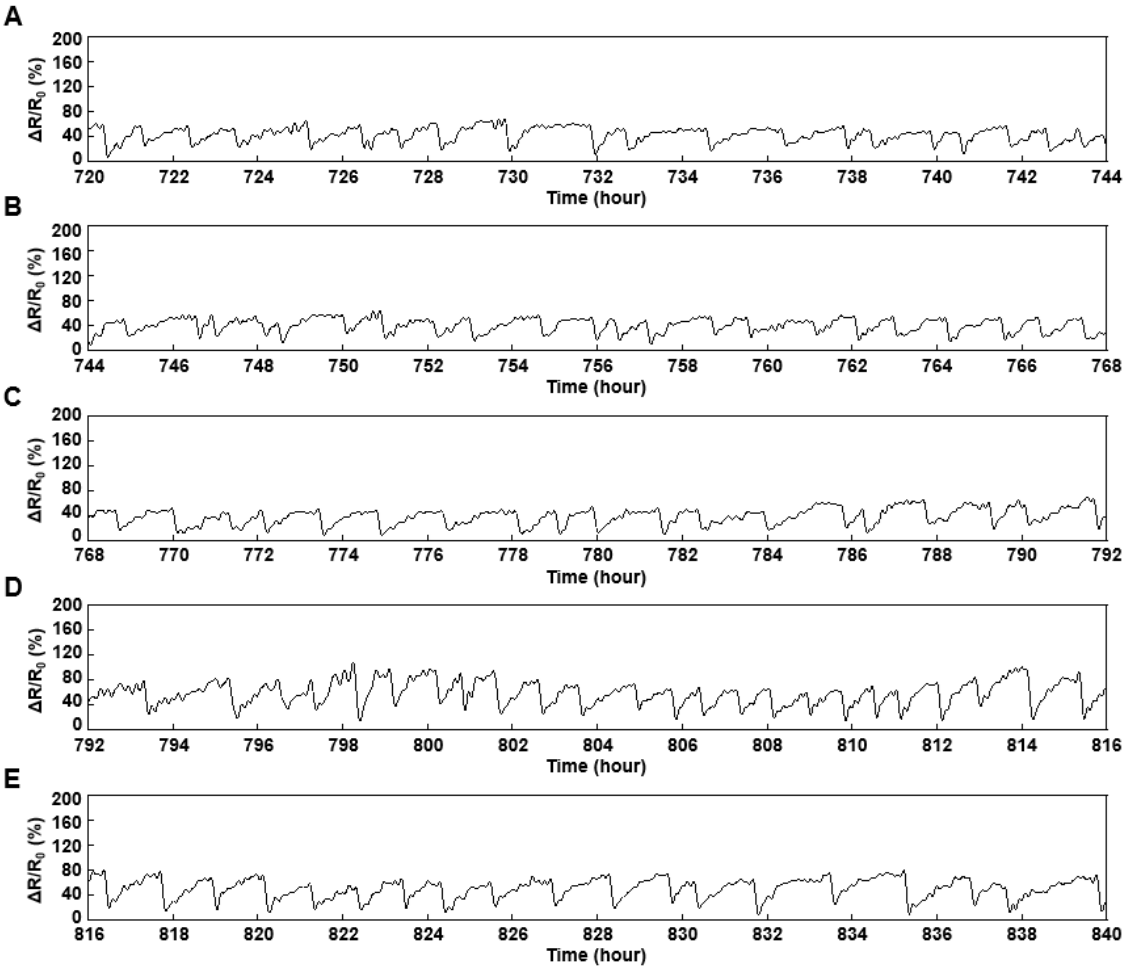

Fig. S27. Relative change in the resistance of the strain gauge from 720 h to 840 h post-surgery.

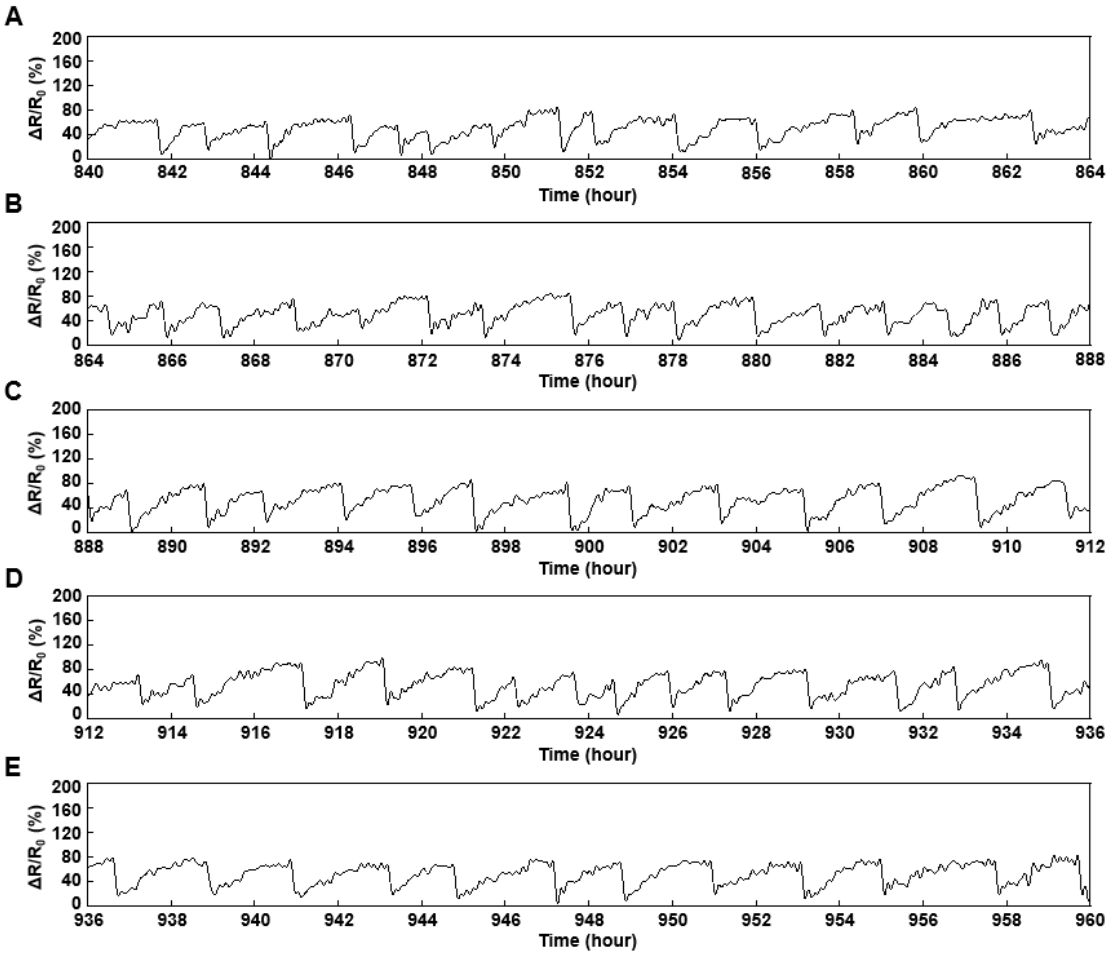

Fig. S28. Relative change in the resistance of the strain gauge from 840 h to 960 h post-surgery.

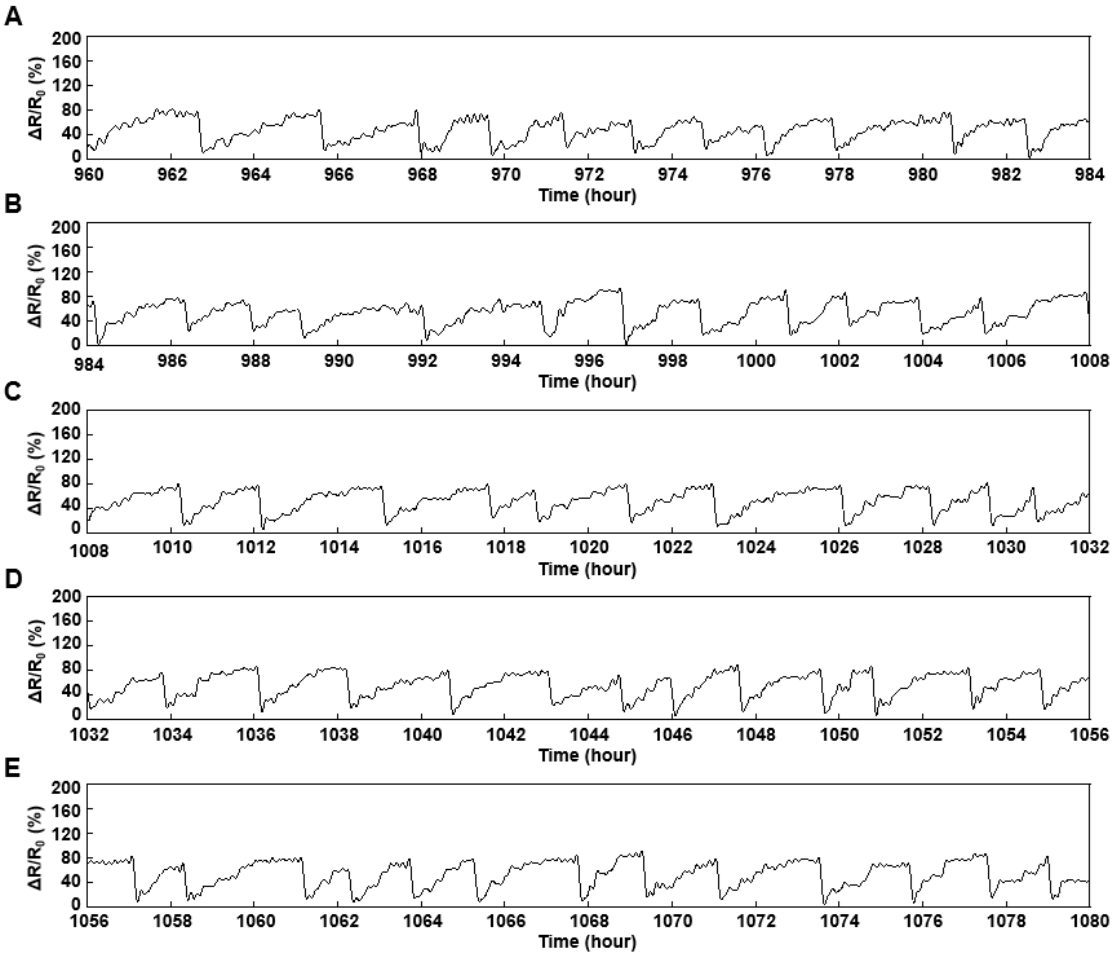

Fig. S29. Relative change in the resistance of the strain gauge from 960 h to 1080 h post-surgery.

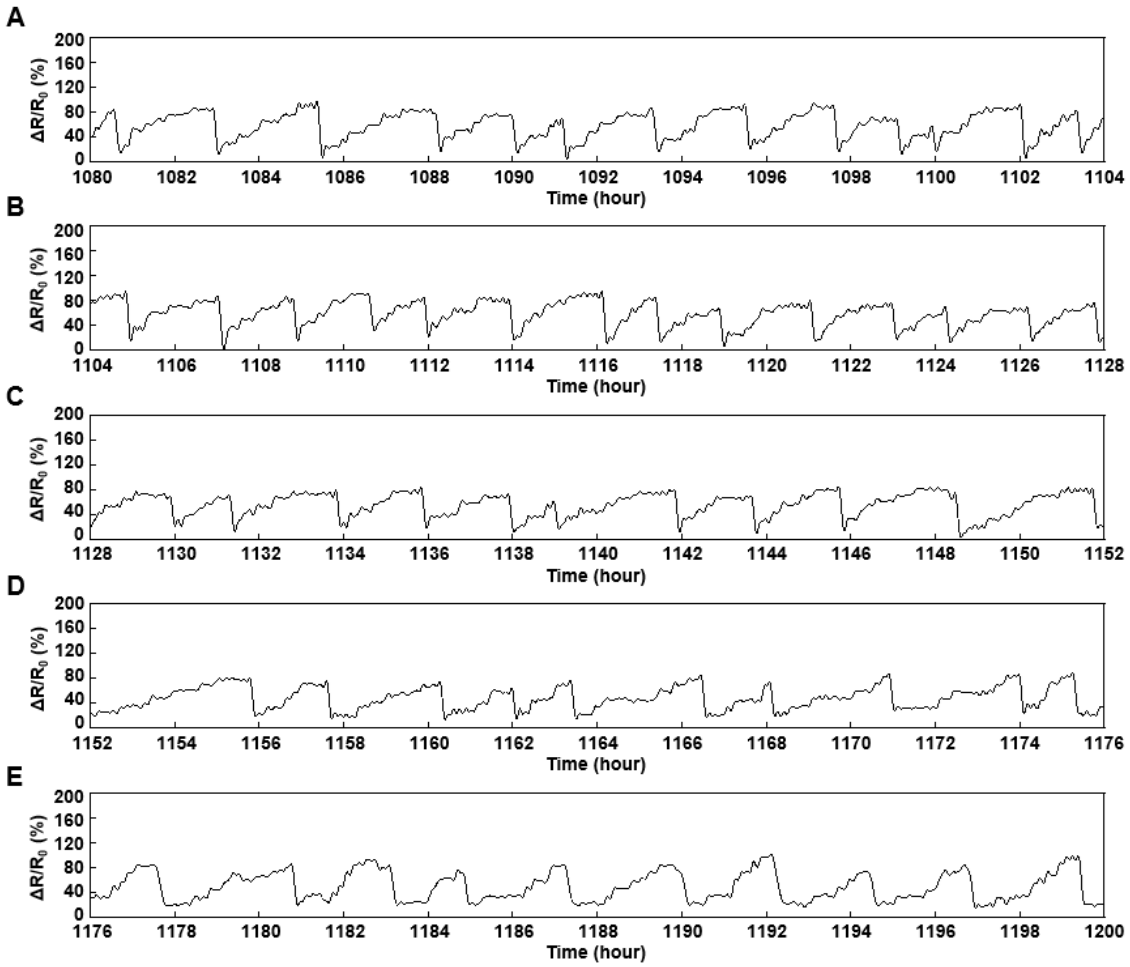

Fig. S30. Relative change in the resistance of the strain gauge from 1080 h to 1200 h post-surgery.

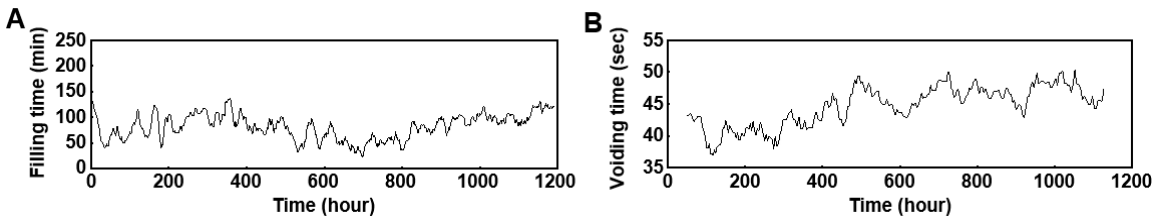

Fig. S31. Chronic studies in non-human primate models. (*A*) Filling and (*B*) voiding times throughout the study.

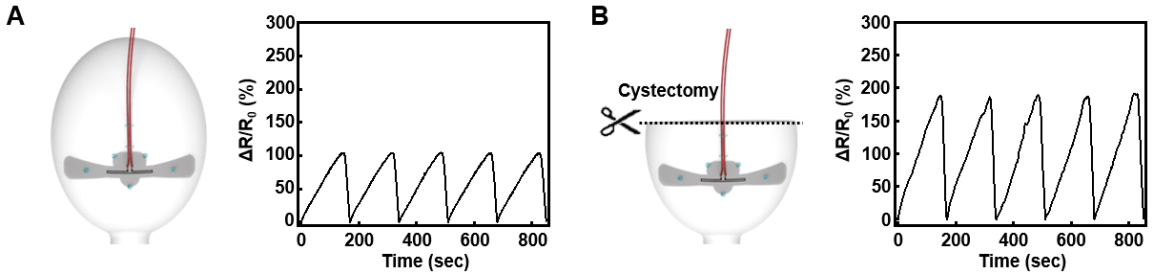

Fig. S32. Results of benchtop tests of (*A*) a normal bladder model and (*B*) a bladder model after partial cystectomy.

Table S1. FEM simulation results for human bladder model.

	First model	Second model	Third model
Strain on strain gauge A (%)	39	51	66
Strain on strain gauge B (%)	89	83	66